Science
AAAS

Supplementary Materials for

p27 Allosterically Activates CDK4 and Antagonizes Palbociclib Inhibition

Keelan Z. Guiley, Jack W. Stevenson, Kevin Lou, Krister J. Barkovich, Vishnu Kumarasamy, Tilini U. Wijeratne, Katharine L. Bunch, Sarvind Tripathi, Erik S. Knudsen, Agnieszka K. Witkiewicz, Kevan M. Shokat, Seth M. Rubin

Correspondence to: srubin@ucsc.edu

This PDF file includes:

Materials and Methods

Western blots and antibodies

Whole-cell extracts from MCF7 (ATCC, HTB-22), MDA-MB-231 (ATCC, HTB-26), T98G (ATCC, CRL-1690), and NIH 3T3 cells (gift from Charles Sherr, St. Jude Children's Research Hospital) were prepared by lysing cells with lysis buffer containing 50 mM Tris pH 7, 150 mM NaCl, 1 mM DTT, 10% glycerol, and 0.1% Tween-20 in the presence of 1X Sigma protease inhibitor cocktail. Whole-cell extracts were either used for endogenous kinase assays or combined with 2X SDS-loading buffer for western blot analysis.

For western blot analysis of endogenous kinase assay input, GAPDH (SCBT G-9), PPIB (Thermo Fisher, PA1-027A) and CycD1 (abcam, EPR2241) antibodies were used. Proteins were resolved by SDS-PAGE and transferred to nitrocellulose membranes, which were then incubated with primary antibodies at 4°C overnight, followed by incubation with HRP-tagged anti-mouse or anti-rabbit secondary antibodies at room temperature up to 1 hr. Pierce ELC Western Blotting Substrate kit (Thermo Fisher, 32106) was used to detect the immuno-reactive bands.

Western blots for XO44 experiments were performed with quenched click reaction solutions prepared as described in "XO44 labeling assays" in the main text. Solutions containing 25 µg protein were resolved by SDS-PAGE on 4-12% BT gels (Invitrogen) at 200 V for 1 hr in MES buffer and transferred to 0.45-µM nitrocellulose membranes, which were then incubated with primary antibodies at 4˚C overnight, followed by incubation with LI-COR IRDye anti-mouse and anti-rabbit secondary antibodies at room temperature for 1 hr. Bands were imaged on a LI-COR Odyssey scanner.

For the CycD1 and CycE1 immunoprecipitations, cells were lysed in immunoprecipitation lysis buffer (20 mM Tris-HCl pH 8.0, 2 mM EDTA, 137 mM NaCl, 1% NP-40) in the presence of 1X Halt protease inhibitor (Thermo Fisher) and 1 mM PMSF. 0.5-0.8 mg of protein from the lysates was incubated with 5 µg of anti-CycD1 (Invitrogen; MA5-12707) or anti-CycE1 (Santa Cruz Biotechnology; SC-377100) and with mouse IgG1 isotype control (Cell Signaling Technology, 5415) at 4°C overnight. Protein immunocomplexes were then incubated with protein G-agarose (Thermo Fisher) at 4°C up to 4 hour and were then washed 3 times with IP wash buffer (20 mM Tris-HCl, pH 8.0, 100 mM NaCl, 0.5% NP-40). Complexes bound to protein G-agarose were eluted using 2X SDS buffer and subjected to immunoblot analysis. Antibodies for western blot detection were used at 1:1000 dilution and were as follows: CDK4 (12790S), CDK2 (2546S), CycE1 (4129S), Rb phosS780 (9307L), Rb phosS807/811 (8516S), p21 (2947S), and p27 (2552S) were purchased from Cell Signaling. CycD1 (SC20044) was purchased from Santa Cruz Biotech.

Western blots for gel filtration assays were performed as for XO44 experiments but SDS-PAGE gels were run in MOPS buffer for 50 min. Fractions on which the XO44 click reaction was performed were handled as for XO44 experiments. Primary antibodies for XO44 and gel filtration assays were obtained for CDK4 (CST 12790), p27 (3686), p18 (2896), CycD1 (2978), CycD3 (2936), Cdc37 (4793), Aurora B (3094), α-tubulin (3873), CDK2 (Bio-Rad VMA00126), and Hsp90 (SCBT 13119) and used at 1:1000 dilution.

Synthesis of palbociclib-biotin

Nuclear magnetic resonance (NMR) spectra were recorded on a Varian spectrometer at 400 MHz or on a Bruker spectrometer at 500 MHz. Chemical shifts were reported as parts per million (ppm) from solvent references. Liquid chromatography-mass spectrometry (LC-MS) was performed on a Waters Xevo G2-XS QTof (0.6 mL/min) using an ACQUITY UPLC BEH C18 column (Waters) and a water/acetonitrile gradient (0.05 % formic acid) using Optima LC-MS grade solvents (Fisher Scientific). All other solvents were of ACS grade (Fisher Scientific, Millipore Sigma) and used without further purification. Palbociclib was obtained from LC Laboratories and biotin-PEG4-acid was obtained from BroadPharm. Commercially available reagents were used without further purification. Analytical thin-layer chromatography was performed with silica gel 60 F254 glass plates (Millipore Sigma). Silica gel chromatography was performed with RediSep Rf normal-phase silica flash columns using a CombiFlash Rf+ (Teledyne ISCO).

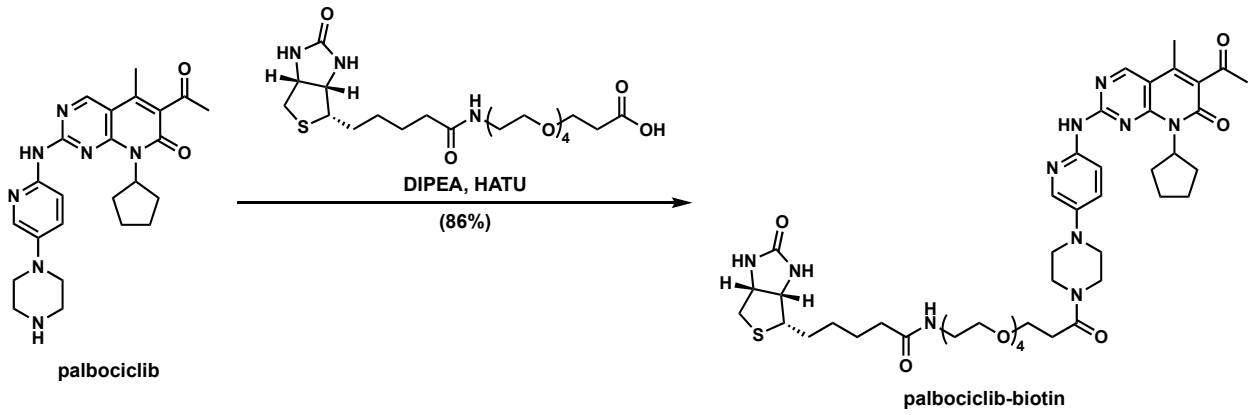

Palbociclib-biotin. A reaction vessel was charged with palbociclib (30 mg, 0.0670 mmol) and biotin-PEG4-acid (36 mg, 0.0737 mmol). Dimethylformamide (335 µL), N,N-diisopropylethylamine (35 µL, 0.201 mmol), and HATU (38 mg, 0.101 mmol) were added and the reaction was stirred at room temperature overnight. The mixture was concentrated *in vacuo*. The crude mixture was purified by flash

chromatography over silica gel eluting with a gradient from 0% methanol-dichloromethane to 20% methanol-dichloromethane to afford palbociclib-biotin (53 mg, 0.0575 mmol, 86% yield) as a yellow semisolid.

^{1}H NMR (400 MHz, DMSO-d_6): δ 10.14 (s, 1H), 8.95 (s, 1H), 8.07 (d, *J* = 2.7 Hz, 1H), 7.88 (d, *J* = 9.0 Hz, 1H), 7.83 (t, *J* = 5.4 Hz, 1H), 7.49 (dd, *J* = 9.1, 2.8 Hz, 1H), 6.42 (s, 1H), 6.36 (s, 1H), 5.82 (p, *J* = 8.8 Hz, 1H), 4.35 – 4.24 (m, 1H), 4.17 – 4.06 (m, 1H), 3.67 – 3.59 (m, 6H), 3.52 – 3.47 (m, 12H), 3.38 (t, *J* = 5.9 Hz, 2H), 3.22 – 3.14 (m, 4H), 3.13 – 3.05 (m, 3H), 2.84 – 2.77 (m, 1H), 2.63 (t, *J* = 6.5 Hz, 2H), 2.42 (s, 3H), 2.30 (s, 3H), 2.28 – 2.17 (m, 2H), 2.05 (t, *J* = 7.3 Hz, 2H), 1.96 – 1.83 (m, 2H), 1.82 – 1.70 (m, 2H), 1.66 – 1.54 (m, 3H), 1.53 – 1.39 (m, 3H), 1.30 – 1.25 (m, 3H).

^{13}C NMR (126 MHz, DMSO-d_6): δ 202.5, 172.1, 168.9, 162.8, 160.8, 158.5, 158.3, 154.8, 144.8, 143.2, 142.1, 135.9, 129.3, 125.4, 115.0, 106.6, 69.8, 69.7, 69.6, 69.2, 66.8, 61.1, 59.2, 55.5, 52.9, 48.9, 48.4, 44.8, 40.7, 38.5, 35.1, 32.8, 31.4, 28.2, 28.1, 27.6, 25.3, 25.2, 13.7.

HRMS (ESI-TOF): *m/z*: calculated for $C_{45}H_{65}N_{10}O_9S$ $[M + H]^+$ 921.4651, found 921.4646

TLC: R_f = 0.6 (20% methanol-dichloromethane)

Synthesis of XO-nc

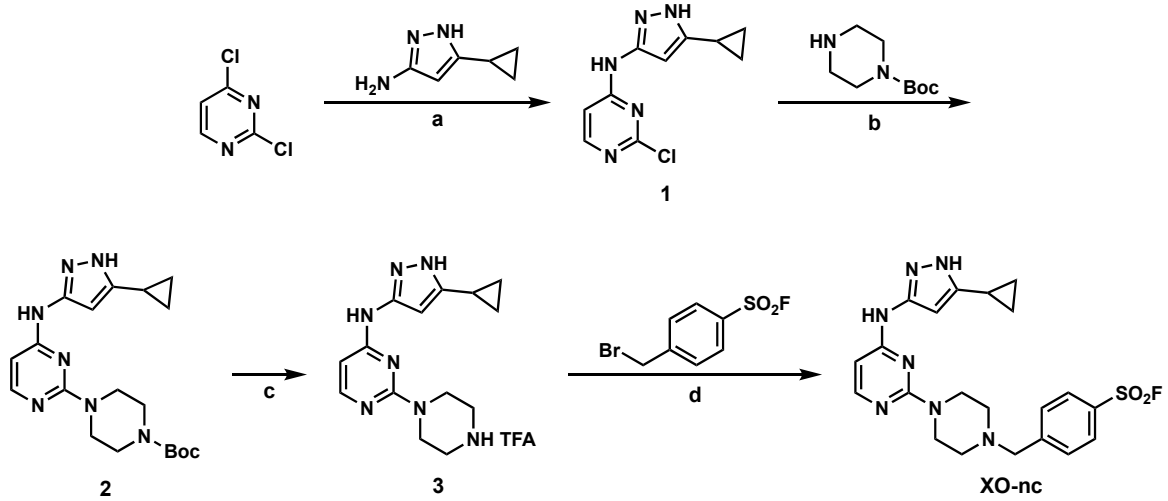

Reagents and conditions. (a) 3-amino-5-cyclopropyl-1*H*-pyrazole, DIPEA, EtOH (43%). (b) 1-Boc-piperazine, DMF (40%). (c) TFA, CH_2Cl_2 (98%). (d) 4-(bromomethyl)benzenesulfonyl fluoride, DIPEA, DMF (67%). The synthesis of XO-nc is based upon that reported for XO44 in Q. Zhao *et al.*, *J. Am. Chem. Soc.* **139**, 680–685 (2017).

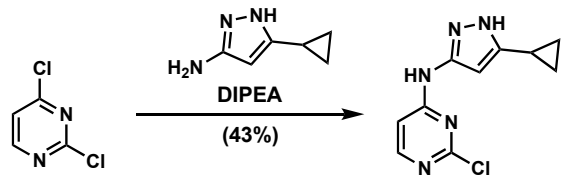

1

Compound 1. A reaction vessel was charged with 3-amino-5-cyclopropyl-1*H*-pyrazole (1.35 g, 11.0 mmol) and 2,4-dichloropyrimidine (1.49 g, 10.0 mmol). Ethanol (10 mL) and *N*,*N*-diisopropylethylamine (2.61 mL, 15.0 mmol) were added and the reaction was stirred at 60 °C overnight. The mixture was cooled to room temperature and poured over 50 mL of ice-cold water. The precipitated solid was filtered and washed with an additional 100 mL of ice-cold water. The filtered solid was dried *in vacuo* to afford compound 1 (1.01 g, 4.29 mmol, 43% yield) as a light pink solid.

^{1}H NMR (400 MHz, DMSO-d_6) δ 12.18 (s, 1H), 10.27 (s, 1H), 8.15 (s, 1H), 7.31 (s, 1H), 5.93 (s, 1H), 1.94 – 1.83 (m, 1H), 0.97 – 0.87 (m, 2H), 0.71 – 0.65 (m, 2H).

^{13}C NMR (100 MHz, DMSO) δ 160.8, 159.3, 157.9, 147.2, 146.0, 104.8, 92.7, 7.8, 6.7.

HRMS (ESI-TOF): *m/z*: calculated for $C_{10}H_{11}ClN_5$ $[M + H]^+$ 236.0697, found 236.0711

TLC: R_f = 0.3 (ethyl acetate)

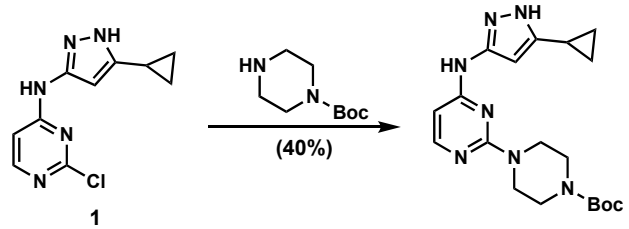

1 2

Compound 2. A reaction vessel was charged with compound 1 (200 mg, 0.849 mmol) and 1-Boc-piperazine (316 mg, 1.70 mmol). Dimethylformamide (0.849 mL) was added and the reaction was stirred at 100 °C for 2 h. The mixture was partitioned between ethyl acetate and 5% citric acid. The organic layer was washed with saturated sodium bicarbonate, water (4X), and brine (2X), dried over magnesium chloride, filtered, and concentrated *in vacuo*. The crude was purified by flash chromatography over silica gel eluting with a gradient from 50% ethyl acetate-hexanes to 100% ethyl acetate to afford compound 2 (130 mg, 0.337 mmol, 40% yield) as a white solid.

^{1}H NMR (400 MHz, DMSO-d_6) δ 11.93 (s, 1H), 9.38 (s, 1H), 7.89 (d, J = 5.7 Hz, 1H), 6.32 (s, 1H), 6.04 (s, 1H), 3.71 – 3.62 (m, 4H), 3.42 – 3.33 (m, 4H), 1.93 – 1.83 (m, 1H), 1.42 (s, 9H), 0.95 – 0.88 (m, 2H), 0.69 – 0.64 (m, 2H).

^{13}C NMR (100 MHz, DMSO-d_6) δ 161.1, 159.8, 156.0, 154.0, 147.9, 145.8, 96.3, 92.4, 79.0, 43.2, 43.1, 28.1, 7.8, 6.9.

HRMS (ESI-TOF): *m/z*: calculated for $C_{19}H_{28}N_7O_2$ $[M + H]^+$ 386.2299, found 386.2303

TLC: R_f = 0.6 (ethyl acetate)

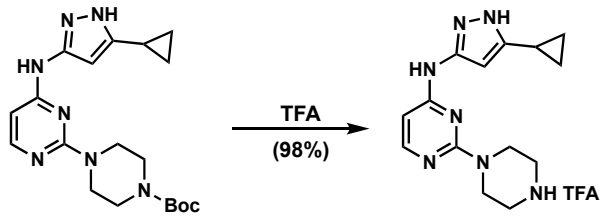

2 3

Compound 3. A reaction vessel was charged with compound 2 (1.28 g, 3.31 mmol). Dichloromethane (3 mL) and trifluoroacetic acid (3 mL) were added and the reaction was stirred at room temperature for 1 h. The mixture was concentrated *in vacuo* and diethyl ether was added to the resulting oil. Sonication resulted in the formation of a solid precipitate that was filtered and washed with additional diethyl ether. The filtered solid was dried *in vacuo* to afford compound 3 (1.30 g, 3.26 mmol, 98% yield) as a white solid.

HRMS (ESI-TOF): *m/z*: calculated for $C_{14}H_{20}N_7$ $[M + H]^+$ 286.1775, found 286.1788

TLC: R_f = 0.0 (ethyl acetate)

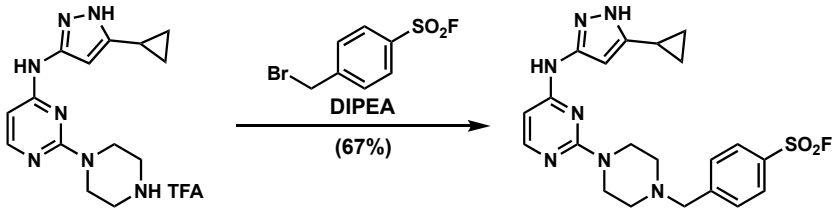

3 XO-nc

XO-nc. A reaction vessel was charged with compound 3 (100 mg, 0.250 mmol) and 4-(bromomethyl)benzenesulfonyl fluoride (70 mg, 0.275 mmol). Dimethylformamide (0.5 mL) and *N*,*N*-diisopropylethylamine (131 µL, 0.751 mmol) were added and the reaction was stirred at room temperature for 20 min. The mixture was partitioned between ethyl acetate and saturated sodium bicarbonate. The

organic layer was washed with water (4X) and brine (2X), dried over magnesium sulfate, filtered, and concentrated *in vacuo*. The crude was purified by flash chromatography eluting with a gradient form 50% ethyl acetate-hexanes to 100% ethyl acetate to afford XO-nc (77 mg, 0.168 mmol, 67% yield) as a white solid.

^{1}H NMR (400 MHz, DMSO-d_6) δ 11.91 (s, 1H), 9.35 (s, 1H), 8.11 (d, J = 8.4 Hz, 2H), 7.87 (d, J = 5.7 Hz, 1H), 7.76 (d, J = 8.2 Hz, 2H), 6.30 (s, 1H), 6.04 (s, 1H), 3.75 – 3.69 (m, 4H), 3.68 (s, 2H), 2.48 – 2.38 (m, 4H), 1.89 – 1.80 (m, 1H), 0.93 – 0.85 (m, 2H), 0.67 – 0.60 (m, 2H).

^{13}C NMR (100 MHz, DMSO-d_6) δ 161.2, 159.7, 156.0, 148.3, 147.9, 145.7, 130.3, 129.9 (d, J = 23.1 Hz), 128.5, 96.1, 92.4, 61.1, 52.6, 43.5, 7.8, 6.9.

HRMS (ESI-TOF) *m/z*: calculated for $C_{21}H_{25}FN_7O_2S$ $[M + H]^+$ 458.1769, found 458.1775

TLC: Rf: 0.4 (ethyl acetate)

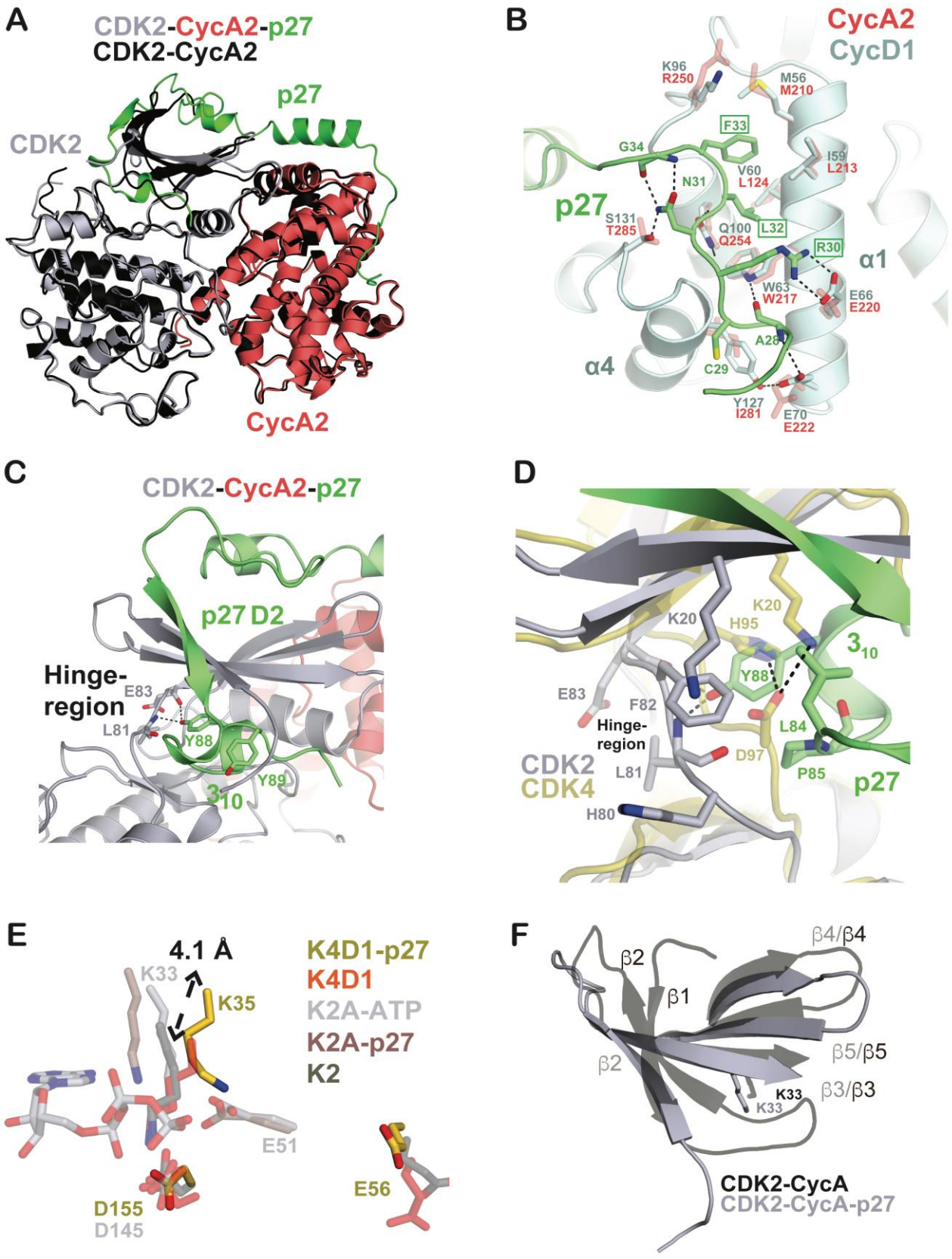
A
CDK2-CycA2-p27
CDK2-CycA2
p27
CDK2
CycA2
B
CycA2
CycD1
K96
R250
M56
M210
F33
G34
I59
L213
V60
L124
N31
p27
S131
T285
Q100
Q254
L32
R30
α1
W63
W217
E66
E220
A28
α4
C29
Y127
I281
E70
E222
C
CDK2-CycA2-p27
p27 D2
Hinge-
region
E83
L81
Y88
Y89
3 10
D
K20
K20
H95
3 10
Y88
E83
F82
Hinge-
region
L84
D97
CDK2
CDK4
L81
P85
p27
H80
E
4.1 Å
K33
K35
K4D1-p27
K4D1
K2A-ATP
K2A-p27
K2
E51
E56
D155
D145
F
β4/β4
β2
β1
β5/β5
β2
K33
β3/β3
K33
CDK2-CycA
CDK2-CycA-p27

Fig. S1 Comparison of how p27 binds and changes the structures of CDK4-CycD1 and CDK2-CycA. **(A)** Alignment of the CDK2-CycA2 dimer (black, PDB code: 1JST) and p27-CDK2-CycA2 trimer (colored, PDB code: 1JSU) structures. Unlike the case for CDK4-CycD1 (**Fig. 3, A through D**), association of p27 does not change the relative orientation of the CDK2 and CycA domains. **(B)** Comparison of p27 interactions with the hydrophobic clefts in CycD1 and CycA2. F33 and L32 on p27 dock into hydrophobic pockets in CycD1 formed by the α1 MVRIL helix. R30 on p27 forms a salt-bridge with CycD1 E66 at the N-terminus of the MVRIL helix. The CycD1 W63 indole also forms a hydrogen bond with the carbonyl of p27 A28. CycD1 Q82 forms a hydrogen bond with the carbonyl and amide of R30 and L32 respectively. S131 on CycD1 positions N31 on p27 through a hydrogen bond to form an intramolecular hydrogen-bonding network with the amide and carbonyl of G34. This network stabilizes the p27 loop conformation at the C-terminus of the RxL motif. While many of these interactions are also present between p27 and CycA, a notable difference is Y127 on α4 of the cyclin-box domain of CycD1, which hydrogen bonds and positions E70 on α1 to form a hydrogen bond with the amide of p27 A28. Y127 also makes van der Waals interactions with C29 on p27. Overall, the similar interactions with CycA and CycD explain the previous observation that p27 D1 domain deletion results in a similar loss in affinity of p27 for either CDK2-CycA or CDK4-CycD1 (*79*). **(C)** Similar to how p27 binds CDK4, p27 displaces the β1 strand of CDK2 such that the ATP-binding G loop is not formed. Unlike its binding to CDK4, p27 binds the CDK2 active site by inserting a small 3_{10} helix into the ATP site (*30*). **(D)** Differences in the CDK4 hinge region from CDK2 suggest that 3_{10}-helix insertion of p27 into the CDK4 active site would be sterically hindered. This comparison explains why a 3_{10} helix is not observed in the p27-CDK4-CycD1 structure (**Fig. 1A and Fig. 2D**). The absence of a bound 3_{10} helix is consistent with the observation that 3_{10}-helix deletion does not change the potency of p27 inhibition when measuring CDK4-directed Rb phosphorylation (*79*). (**e**) The reorientation of the N-lobe in CDK4 upon p27 binding moves the CDK4 catalytic lysine (K35) ~4Å and places it in a similar position as the CDK2 catalytic lysine (K33) in the CDK2-CycA structure. In contrast, K35 in the CDK4-CycD1 dimer structure is in a similar position as CDK2 K33 in the structure of inactive CDK2 monomer. (**F**) Unlike in CDK4, the β3-β5 strands of the CDK2 N-lobe do not undergo a conformational change upon p27 binding. In both structures, p27 binding does disrupt the G-loop by displacing the β1 strand.

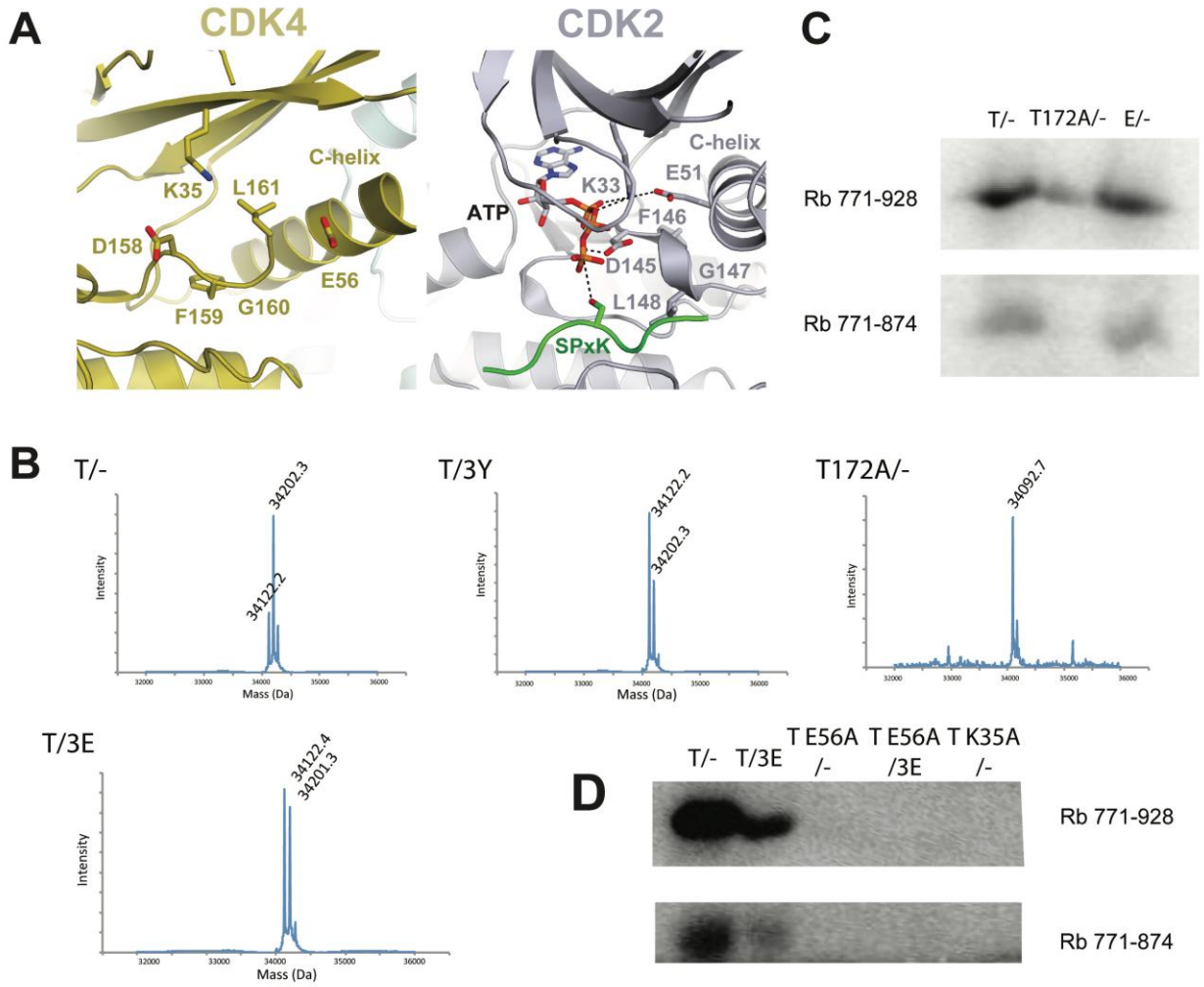

Fig. S2 Characterization of CDK4-CycD1 activation segment and its phosphorylation. (A) Comparison of the activation segment in the p27-CDK4-CycD1 structure (left) and the active CDK2-CycA2 structure with a substrate peptide bound (right, PDB code: 1QMZ). In both structures, the activation segment is released. CDK2 only requires CycA binding for release, while CDK4 also requires p21 or p27 binding. However, in the CDK4 trimer structure, the DFG motif is seen in the inactive "in" conformation and is disordered beyond L161 in the following position. In addition, as in the CDK4-CycD dimer structure, the C-helix is oriented in the inactive "out" conformation, with the critical glutamate pointing away from the active site (*10*, *11*). It may be that substrate binding, ATP binding, or activation segment phosphorylation is also required to generate the DFG "out" conformation and the C-helix "in" conformation. Beyond the position of E56 in the C-helix, other residues in CDK4 that coordinate ATP and are important for catalysis (D99, D140, D158) are in similar position in the p27-CDK4-CycD1 structures as in the active CDK2-CycA structure. **(B)** Electrospray mass spectrometry analysis of recombinant CDK4 samples suggests that p27 inhibits T172 phosphorylation. CDK4-CycD1 expressed in and purified from Sf9 insect cells (T/-) showed ~70% T172 phosphorylation (higher +80 Da species), whereas co-expression with p27 kinase inhibitory domain wild-type (T/3Y) or tyrosine phosphomimetic (T/3E) p27 resulted in ~30%-50% phosphorylation. The homogeneous and unphosphorylated T172A mutant is shown for comparison. Proteins were analyzed with a Sciex X500 QTOF spectrometer. **(C)** Purified wild-type and phosphomimetic (T172E) CDK4 showed greater activity towards Rb 771-928 than a T172A mutant kinase. ^{32}P kinase assay as in **Fig. 3E** is shown but using CDK4-CycD1 dimer complexes with wild-type CDK4 (T/-) or CDK4 with a T172A (T172A/-) or T172E (E/-) mutation to the phosphorylation site in the kinase activation loop.

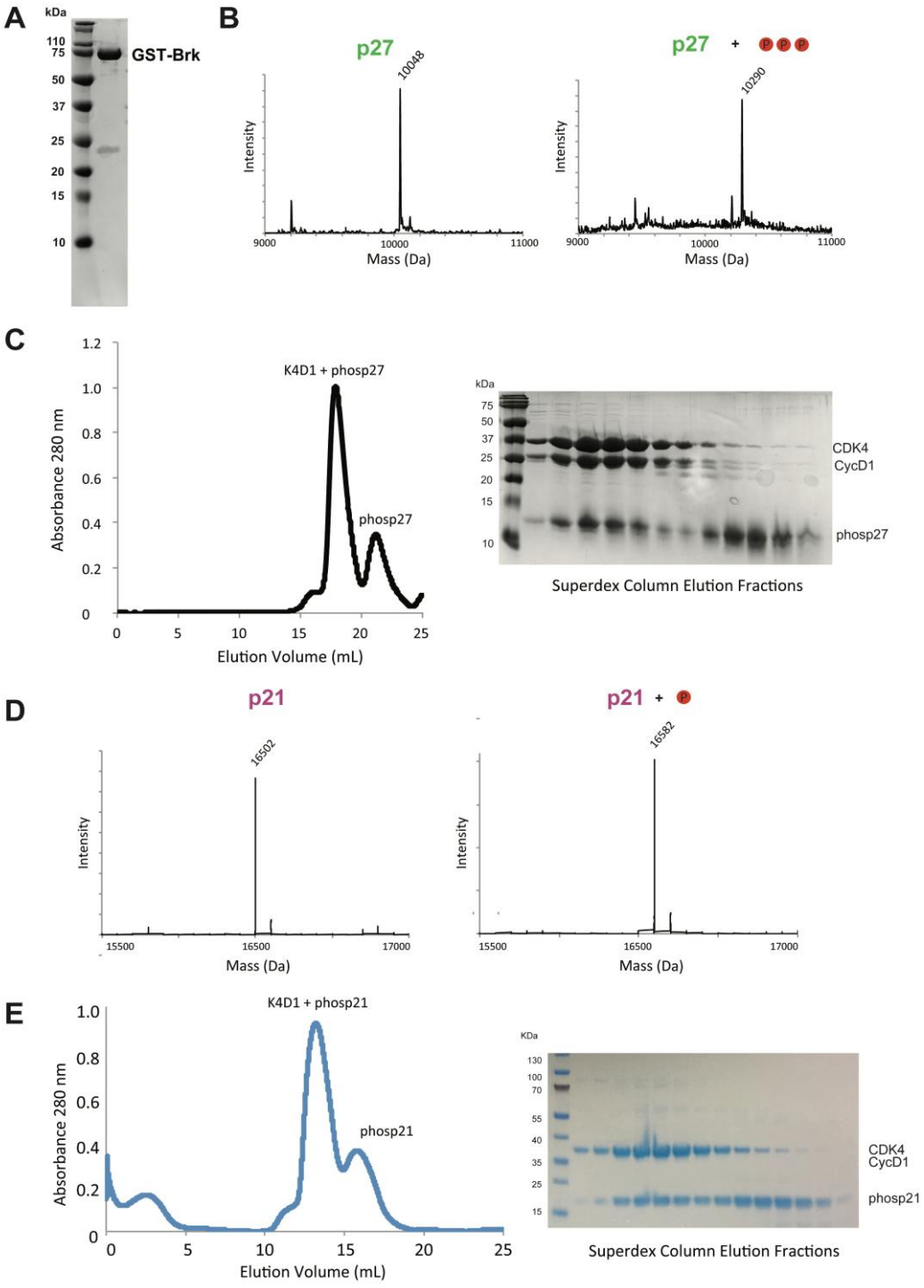

Fig. S3 Preparation of phosp27, phosp21, and reconstituted trimer complexes with CDK4-CycD1. Purified p27 kinase inhibitory domain (KID), full-length p27, and full-length p21 were phosphorylated with recombinant human Brk kinase and added to the CDK4-CycD1 dimer in 3-fold molar excess to form the trimer complex, which was then purified further to separate from Brk and excess p27 or p21. Note that the other trimer complexes characterized here (e.g. with wild-type unphosphorylated p27 and p21 and p27 with

phosphomimetic mutants) were purified following co-expression of all three components. **(A)** Coomassie-stained gel of purified recombinant GST-Brk kinase. **(B)** Electrospray mass spectrometry demonstrates that purified p27 KID (residues 25-93) is phosphorylated on three sites after treatment with GST-Brk, which is consistent with the presence of three tyrosines (Y74, Y88, and Y89) in the sequence. Similar results were obtained for full-length p27. Proteins were run through a C18 reverse phase column in-line with a Sciex X500 QTOF spectrometer. (**C)** Purification of the assembled phosp27($p27^{KID}$; 25-93)-CDK4(ΔG45-G47, G43E, G44E)-CycD1(16-267), trimer using Superdex 200 size-exclusion chromatography. The column is run after mixing a molar of excess phosp27 with purified CDK4-CycD1 dimer. The excess phosp27 elutes as a separate peak. Similar results were obtained with full length and wild-type proteins. **(D)** Electrospray mass spectrometry as in panel **B** demonstrates that purified p21 is phosphorylated on one site after treatment with GST-Brk, which is consistent with the presence of one tyrosine (Y77) in the sequence. (**E)** Purification of the assembled phosp21-CDK4-CycD1 trimer as in panel **C**.

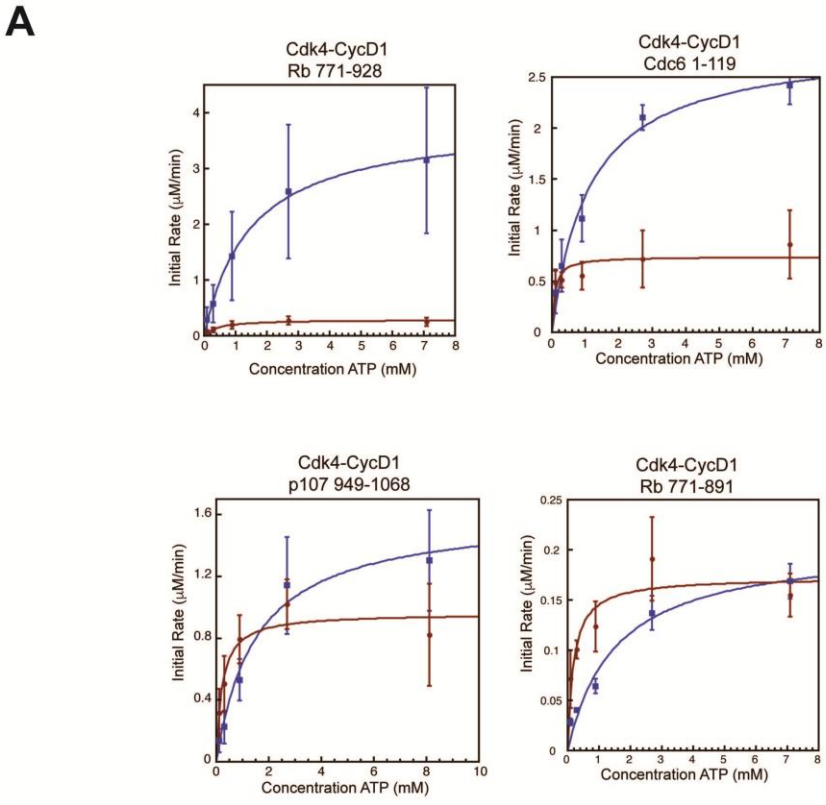

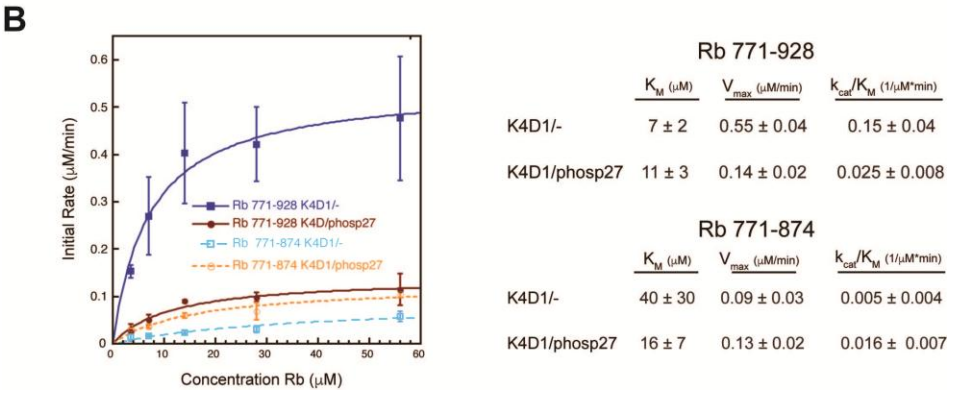

Rb 771-928

	K_M (μM)	V_{max} (μM/min)	k_{cat}/K_M (1/μM*min)
K4D1/-	7 ± 2	0.55 ± 0.04	0.15 ± 0.04
K4D1/phosp27	11 ± 3	0.14 ± 0.02	0.025 ± 0.008

Rb 771-874

	K_M (μM)	V_{max} (μM/min)	k_{cat}/K_M (1/μM*min)
K4D1/-	40 ± 30	0.09 ± 0.03	0.005 ± 0.004
K4D1/phosp27	16 ± 7	0.13 ± 0.02	0.016 ± 0.007

Fig. S4. Data supporting the kinetic analysis of recombinant CDK4 complexes. (A) Steady state kinetic analysis of CDK4-CycD1 activity toward the indicated substrate. The data points and error bars shown in the graphs are the averages and standard deviations, respectively, of initial rates at each concentration point across three replicates. One representative replicate for each ATP titration is shown in **Fig. 3F**. The blue squares are measurements using CDK4-CycD1 dimer with the T172E mutation (K4D1/-); red circles are measurements using the T172E mutant dimer assembled with Brk-phosphorylated p27 (K4D1/phosp27). Fit values for K_M, V_{max}, and k_{cat}/K_M are tabulated in **Fig. 3G**. (**B**) Steady state kinetic assay of Rb phosphorylation by CDK4-CycD1 dimer (K4D1/-) and trimer (K4D1/phosp27), in which Rb substrate concentration is varied. Rb 771-928 and Rb 771-874, which lacks the CycD-docking sequence, were tested. The substrate k_{cat}/K_M is greater for K4D1/- toward Rb 771-928 compared to Rb 771-874 or compared to when the enzyme contains p27. In contrast, the Rb docking sequence does not influence the substrate k_{cat}/K_M for the trimer. These observations are consistent with the presence of a binding site in the enzyme that can be accessed by Rb 771-928 but not Rb 771-874 and that is blocked by p27.

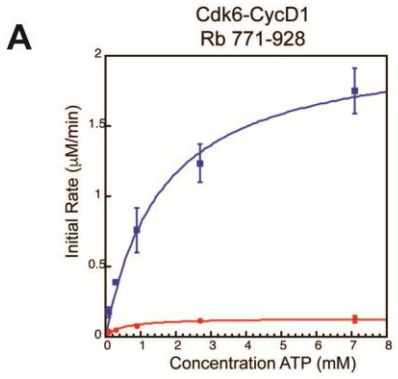

Rb 771-928

	K_M (mM)	V_{max} (μM/min)	k_{cat}/K_M (1/mM*min)
K6D1/-	1.6 ± 0.3	2.1 ± 0.1	1.3 ± 0.2
K6D1/phosp27	0.5 ± 0.01	0.13 ± 0.01	0.3 ± 0.1

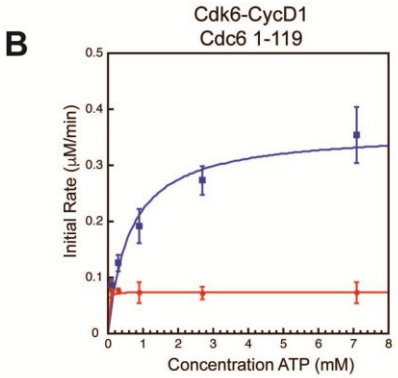

Cdc6 1-119

	K_M (mM)	V_{max} (μM/min)	k_{cat}/K_M (1/mM*min)
K6D1/-	0.6 ± 0.2	0.35 ± 0.03	0.6 ± 0.2
K6D1/phosp27	0.01 ± 0.01	0.074 ± 0.003	7 ± 7

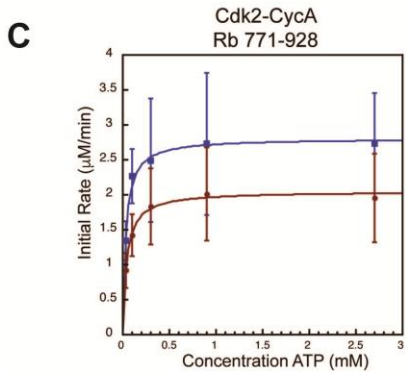

Rb 771-928

	K_M (mM)	V_{max} (μM/min)	k_{cat}/K_M (1/mM*min)
K2A/-	0.032 ± 0.004	2.80 ± 0.07	180 ± 20
K2A/phosp27	0.041 ± 0.004	2.05 ± 0.05	100 ± 10

Fig. S5. Kinetic analysis of recombinant CDK6-CycD1 and CDK2-CycA complexes. Steady state kinetic analysis of CDK6-CycD1 and CDK2-CycA activity toward the indicated substrates. The data points and error bars shown in the graphs are the averages and standard deviations, respectively, of initial rates at each concentration point across three replicates. (**A-B)** The blue squares are measurements using CDK6-CycD1 dimer with a T177E mutation (K6D1/-); red circles are measurements using the T177E mutant dimer assembled with Brk-phosphorylated p27 (K6D1/phosp27). Fit values for K_M, V_{max}, and k_{cat}/K_M are tabulated. (**C**) The blue squares are measurements using CDK2-CycA dimer (K2A/-); red circles are measurements using the dimer assembled with Brk-phosphorylated p27 (K2A/phosp27). In these experiments, CDK2 was unphosphorylated on its activation loop. We note that we observed activity of K2A/phosp27 using recombinant proteins, even though p27-associated kinase activity in cells is thought to arise primarily from CDK4 (*32, 33*). The kinase assay demonstrates that phosphorylated p27 only slightly inhibits K2A activity. This observation is consistent with a recent report that tyrosine phosphorylation dislodges the D2 domain of p27 from CDK2 (*44*). The ATP K_M values measured for the CDK2 dimer and trimer complexes are similar, which is consistent with structural data indicating that CycA is sufficient to organize the ATP-binding site (*9*).

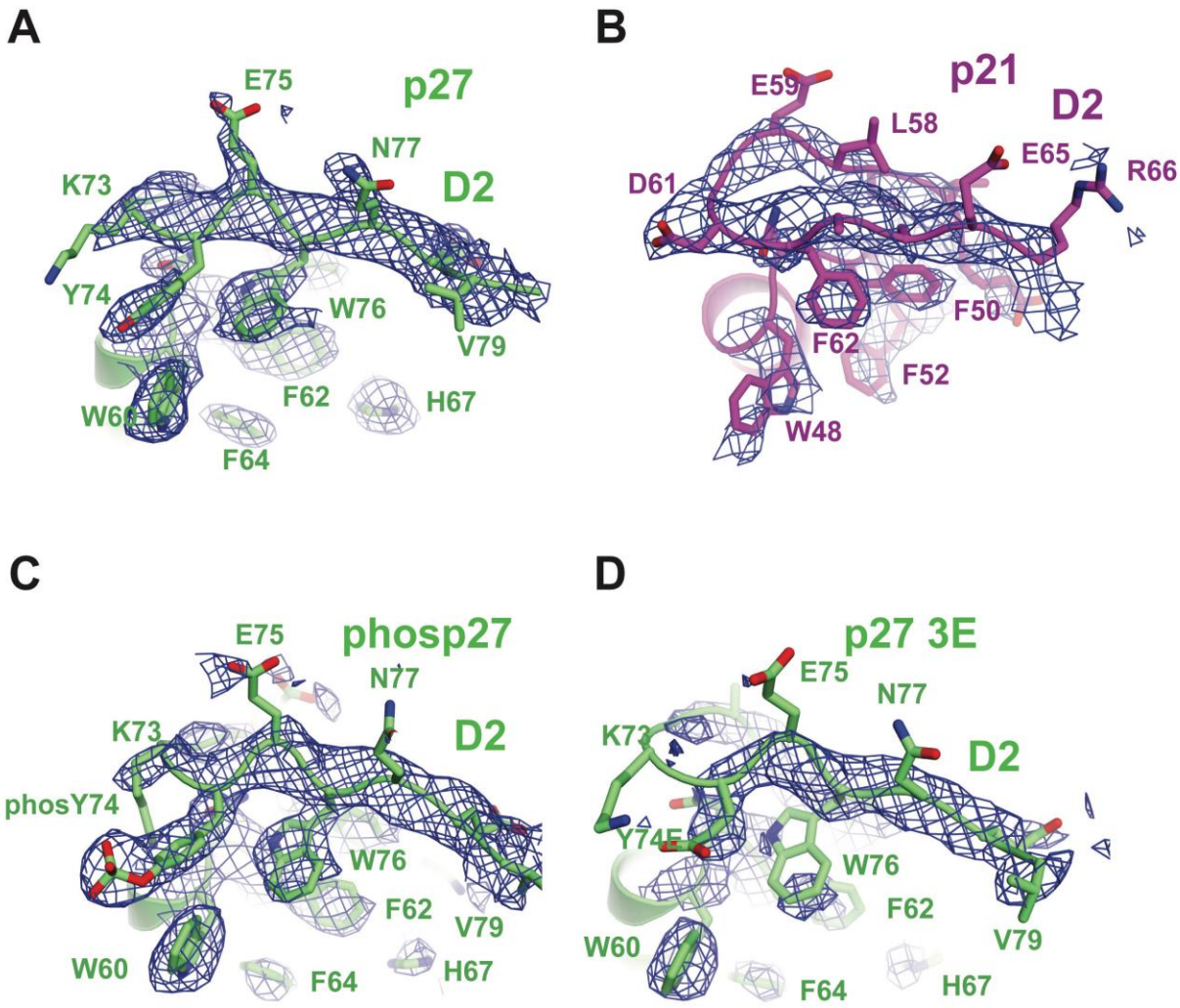

Fig. S6. Representation of electron density for the D2 subdomain. Simulated annealing mFo-DFc omit electron density maps contoured at 2σ. The maps were calculated by removing all atoms in residues 60-79 in p27 or 48-67 in p21□□ Models and maps are shown for CDK4-CycD1 structures with (**A**) unphosphorylated p27, (**B**) unphosphorylated p21, (**C**) phosphorylated p27, and (**D**) 3E mutant p27.

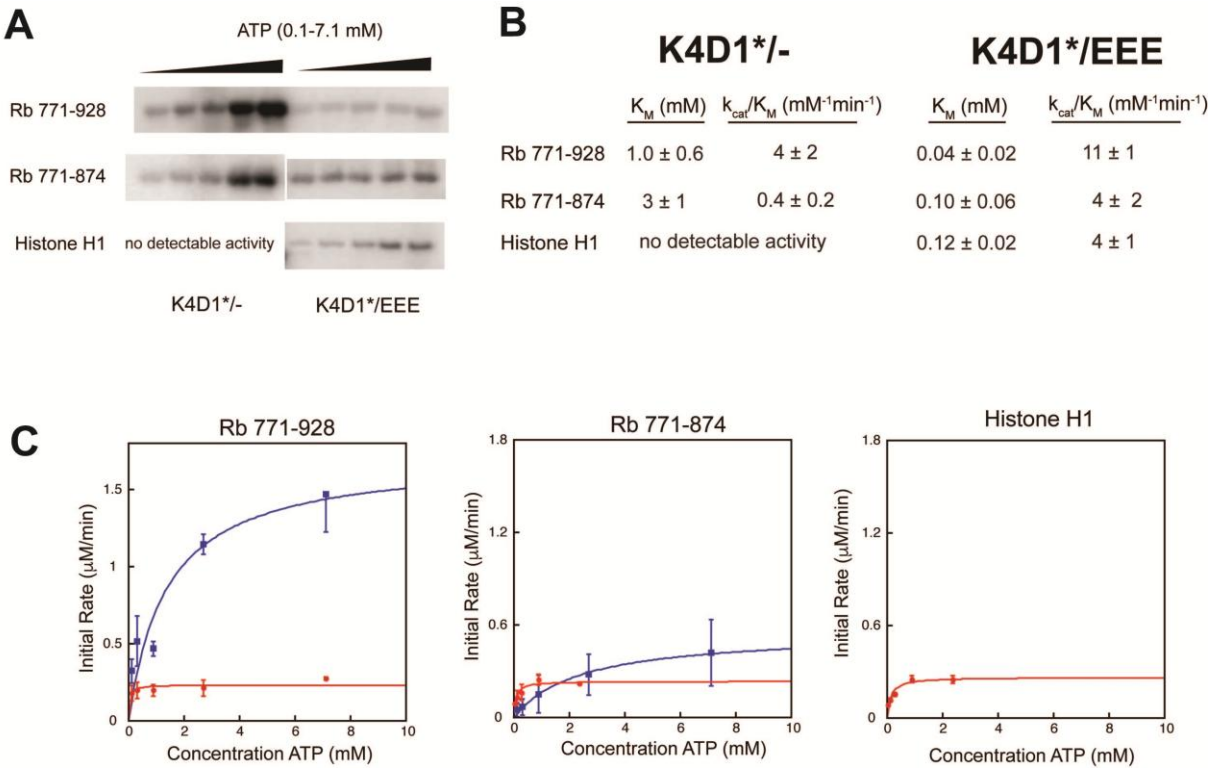

Fig. S7. Phosphomimetic glutamate mutations in p27 activate CDK4 trimer complexes. Steady state kinetic analysis of CDK4-CycD1 as in **Fig. 3, F and G, and Fig. S4** but using the CDK4-CycD1 construct that was crystallized (CDK4 residues 1-303, ΔG45-G47, G43E, G44E; cycD1 residues 16-267; named K4D1*) and using the crystallized phosphomimetic mutant of p27 (p27 residues 25-106, Y74E, Y88E, Y89E). (**A**) Phosphorylation of the indicated substrate with ^{32}P-ATP. (**B**) Fit kinetic parameters. We note that the ATP K_M and k_{cat}/K_M values are similar for the crystallized dimer and the dimer reconstituted from full-length proteins used in **Fig. 3**, indicating that the mutations required for crystallization did not affect enzyme activity. The ATP K_M of the trimer containing the phosphomimetic p27 is less than and the k_{cat}/K_M is greater than the respective values measured for trimer reconstituted with phosp27. We conclude that the phosphomimetic glutamate at Y74 disrupted the D2 domain-CDK4 association more severely than phosphorylation, leading to a more active enzyme. Remarkably, the enzyme with the EEE p27 showed strong activity toward H1, which is thought to be a poor substrate for CDK4 (*11, 12, 14, 15*). We do not propose that this hyperactive phosphomimetic mutation is physiologically relevant, and we do not believe that these data inform whether H1 is a substrate of CDK4 *in vivo*. In fact, we do not observe H1 phosphorylation using the more relevant K4D1/phosp27 enzyme as in **Fig. 3, E and F**. However, these data do support the conclusion that p27 binding increases the activity of CDK4 through structuring the ATP binding site, which is reflected in the reduced K_M and increased catalytic efficiency using this engineered construct. (**C**) Quantification of SDS-PAGE gel data in panel **A** to determine activity toward the indicated substrate. Blue squares are measurements using the CDK4-CycD1 dimer (K4D1*/-), while red circles are measurements made with the p27 phosphomimetic-containing trimer (K4D1*/EEE). The data points and error bars shown in the graphs are the averages and standard deviations, respectively, of initial rates at each concentration point across three replicates.

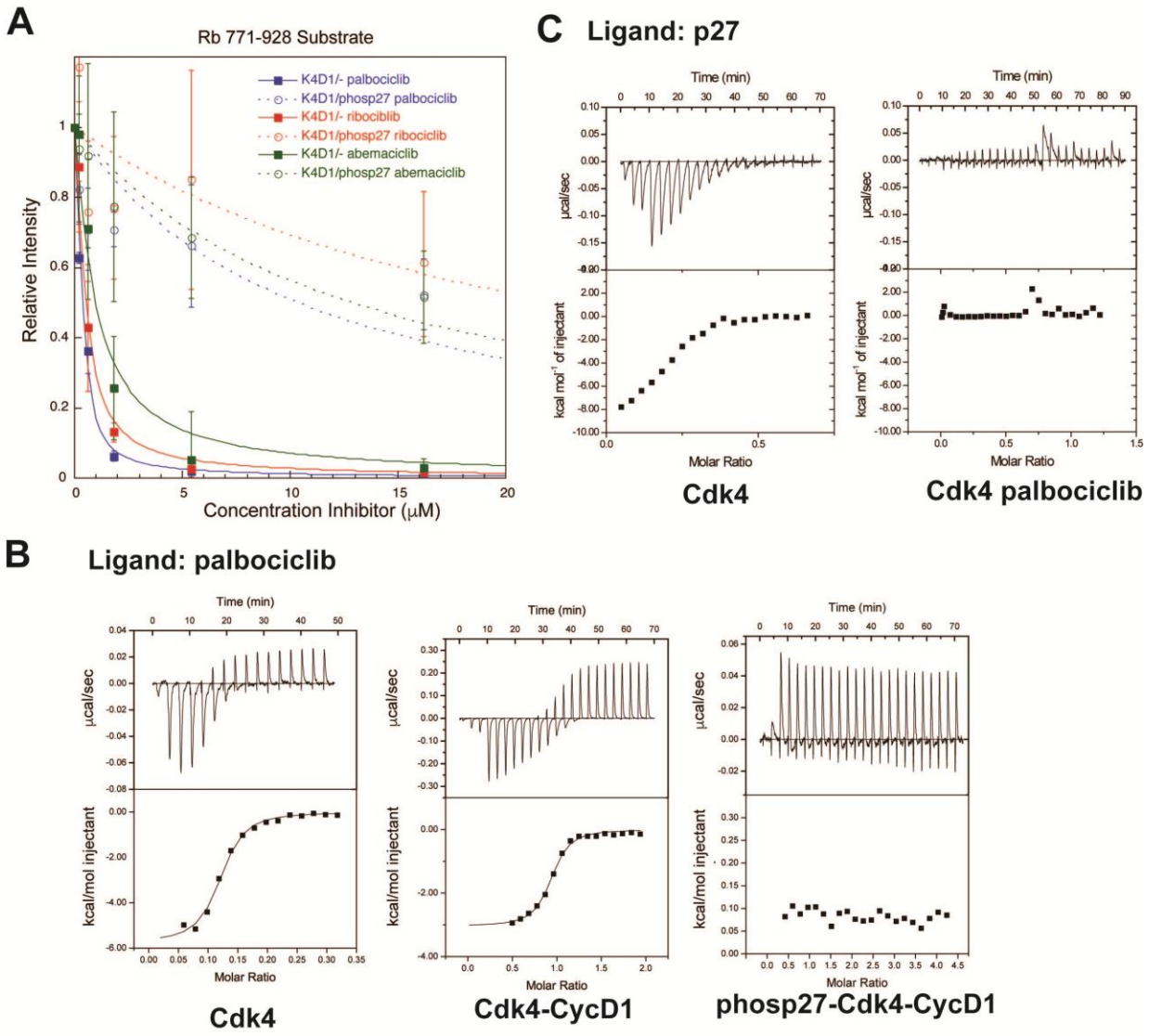

Fig. S8. Data supporting measurements of chemical CDK4 inhibitor interactions with purified recombinant enzymes. (A) Quantification of CDK4-CycD1 dimer (K4D1/-) and trimer (K4D1/phosp27) inhibition by palbociclib (blue), ribociclib (red), and abemaciclib (green) in the enzyme assay shown in **Fig. 5B**. The data points and error bars shown in the graphs are the averages and standard deviations, respectively, of the relative initial rates at each concentration point across three replicates. K_I is calculated from a two-state binding model assuming the bound state has no activity. Experiments were performed with full-length wild-type CDK4, CycD1, and phosphorylated p27. (**B)** Representative ITC data for palbociclib binding to GST-CDK4 monomer, CDK4-CycD1, and phosp27($p27^{KID}$; 25-93)-CDK4-CycD1. The K_d values reported in **Fig. 5C** are averages from three replicates. 0.5 mM palbociclib was titrated into 40 μM GST-CDK4, 40 μM CDK4-CycD1, or 40 μM phosp27($p27^{KID}$; 25-93)-CDK4-CycD1. The measured stoichiometry for palbociclib binding to GST-CDK4 monomer was n ~ 0.2; however, we believe due to the instability of recombinant GST-CDK4 in the ITC cell, the titration underestimated the value of n. Data were collected on a MicroCal VP-ITC calorimeter and data were fit to a one site binding model. (**C**) Representative ITC data for p27($p27^{KID}$; 25-93) binding to 40 μM GST-CDK4 in the absence and presence of 50 μM of palbociclib.

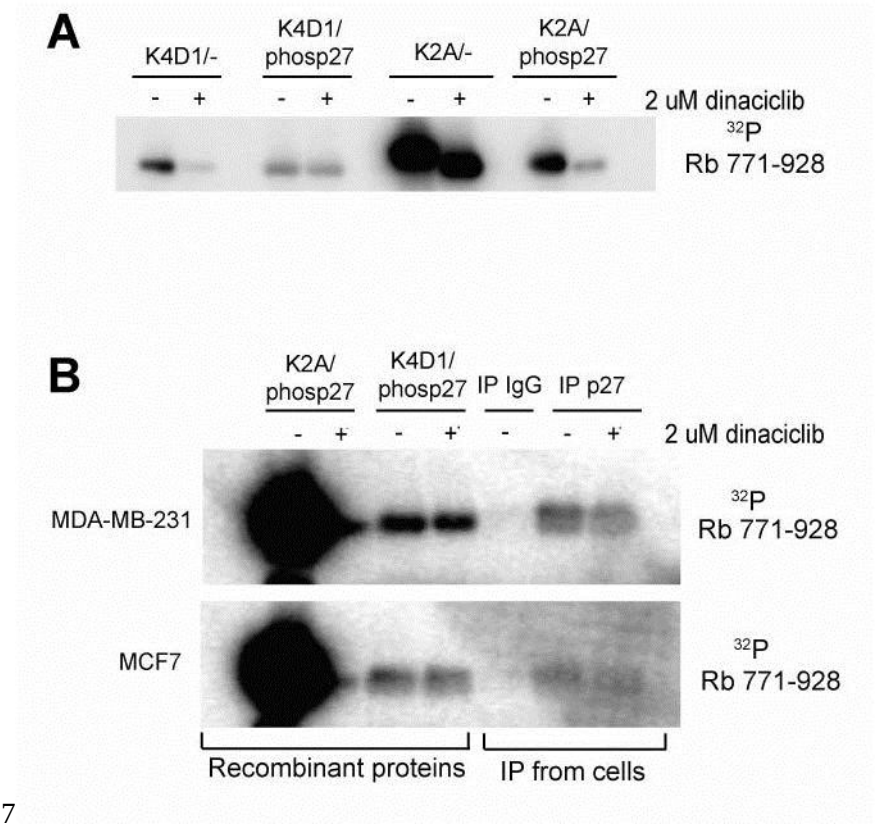

7

Fig. S9. Data supporting kinase activity assays using immunoprecipitated complexes. The kinase activity of p27 immunoprecipitates from MCF7 and MDA-MB-231 cells resembles CDK4 and not CDK2 activity. **(A)** Activity of purified recombinant CDK4-CycD1 (K4D1) and CDK2-CycA (K2A) activity in the absence and presence of phosp27 and dinaciclib. All recombinant complexes were sensitive to the drug at 2 μM except K4D1/phosp27. (**B)** p27-IP on the indicated cell line was performed as in **Fig. 5D,** and the kinase activity was tested in the absence and presence of 2 μM dinaciclib. The assay with recombinant enzymes was included as direct controls in the first four lanes of each gel. Like only the recombinant CDK4 trimer complex activity, the activity from the p27 IP was not sensitive to the drug. We also note that while we did observe *in vitro* activity with recombinant CDK2 trimer complexes here and in **Fig. S5C**, previous data indirectly suggest that CDK2 complexes with p27 in untransformed fibroblast cells have little activity (*32, 33*). Together these data implicate the activity from p27 immunoprecipitates as a CDK4 activity.

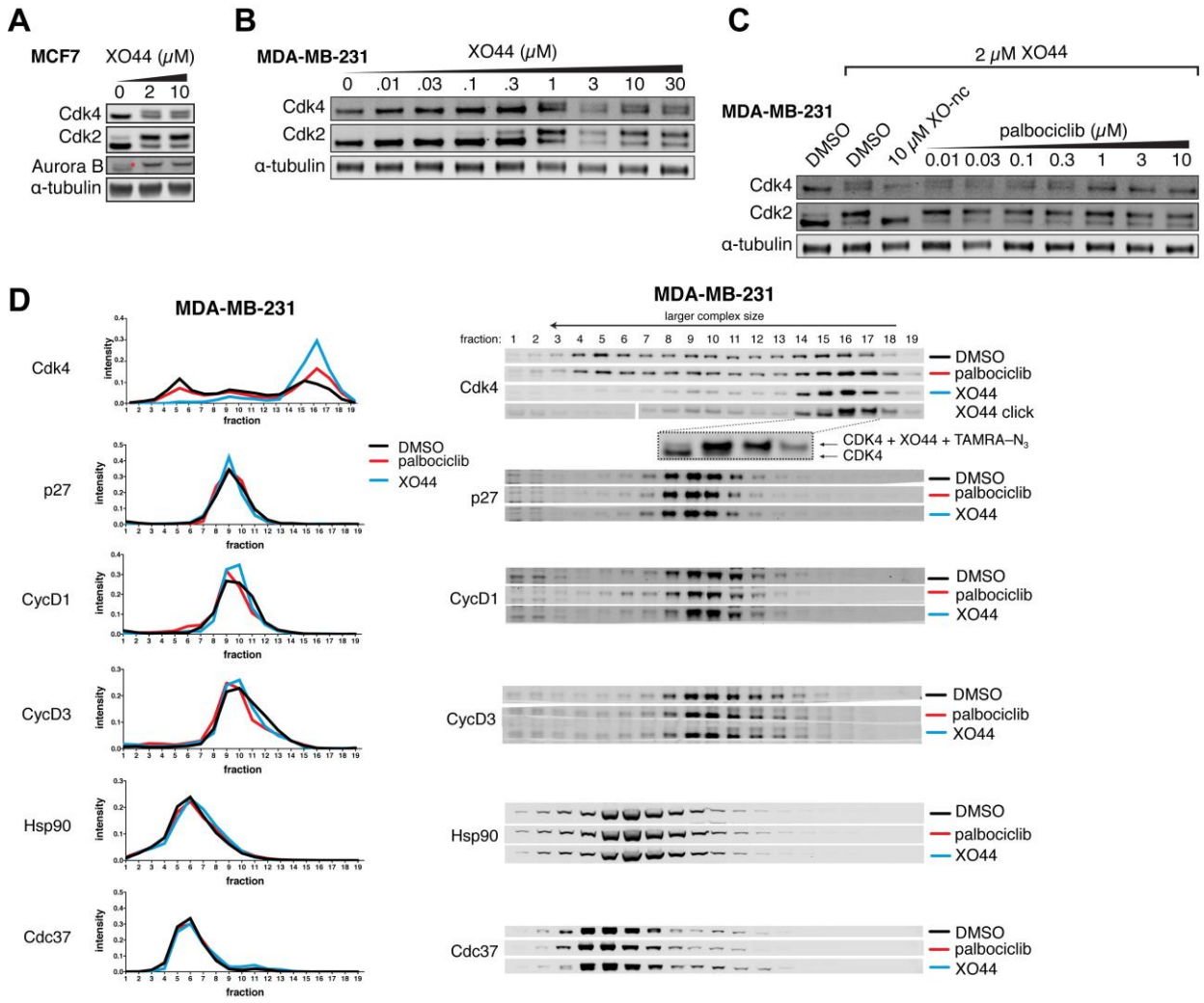

Fig. S10. Data supporting labeling of endogenous CDK4 with XO44. (A) Labeling of endogenous CDK4, CDK2, and Aurora B by the promiscuous covalent ATP-site kinase inhibitor XO44. MCF7 cells were treated with DMSO vehicle or XO44 at the indicated concentrations for 30 min. Lysates were subjected to click reaction with TAMRA–azide to visualize XO44 labeling of proteins by gel mobility shift. The red asterisk represents a nonspecific band in the Aurora B Western blot. **(B)** As in panel **A** and in **Fig. 6A** but experiment was performed in MDA-MB-231 cells. (**C)** Palbociclib competes with XO44 for CDK4 binding but not CDK2 binding. Experiment performed as in **Fig. 6B** but in MDA-MB-231 cells. (**D**) As in **Fig. 6D**, except experiment was performed with MDA-MB-231 cells. Note that the intensity scales vary in the quantification of the blots. The MDA-MB-231 CDK4 XO44 click blot is a single gel but is digitally reordered as shown.

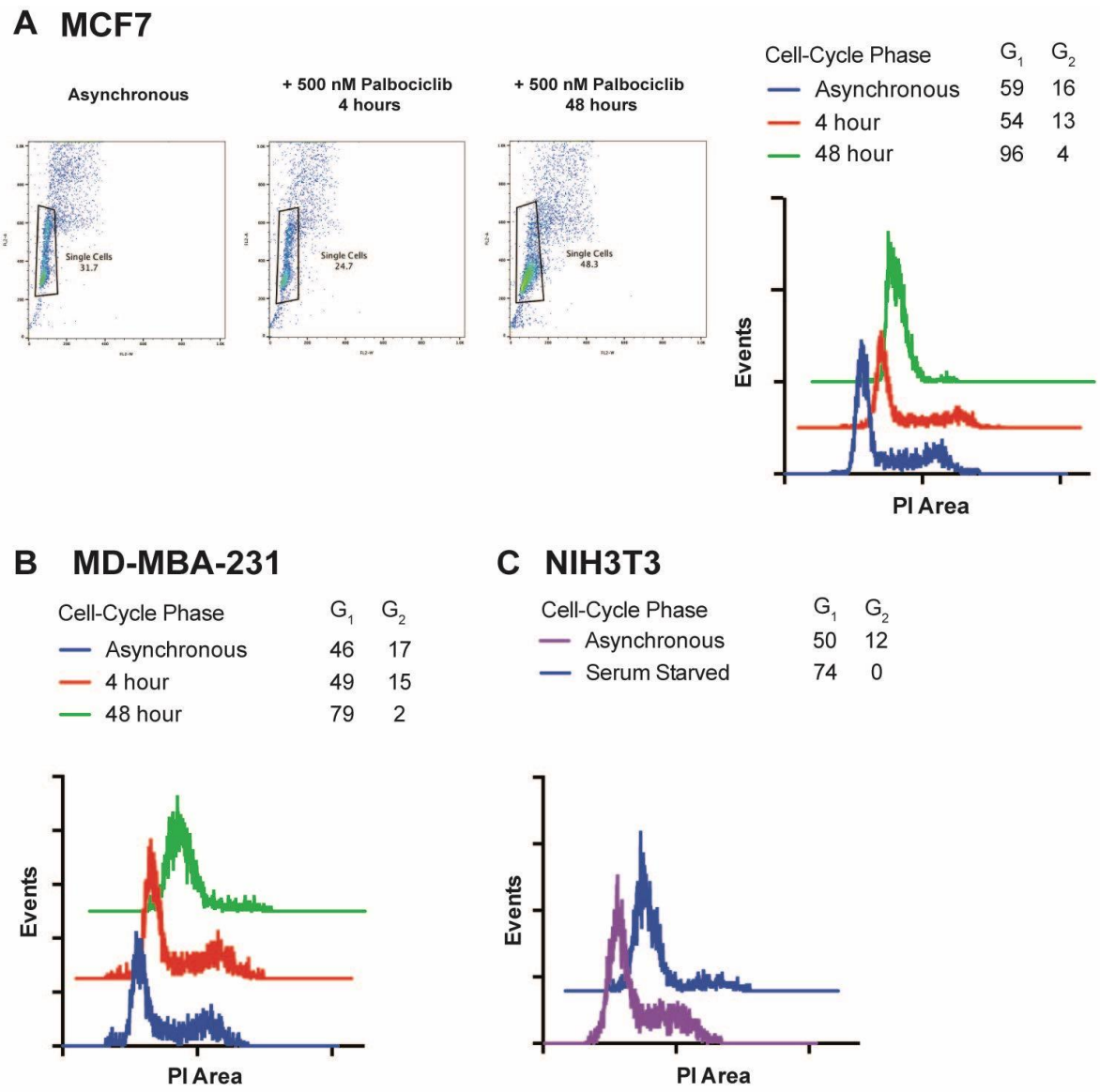

Fig. S11. Propidium iodide staining to demonstrate cell-cycle profile. Cells harvested from 100 mm dishes were washed in PSB and fixed in 70% ethanol. The cells were then incubated in 50 µL of 100 µg/ml RNase A and 200 µL of 50 µg/ml propidium iodide (PI) on ice for 30 minutes. Cells were then analyzed on a BD FACSCalibur instrument and voltage adjusted such that G_1 peak was approximately 300 PI area. Singlets were gated and cell-cycle analysis was performed using FlowJo. Histograms were fit to the Watson Pragmatic algorithm. (**A**) Example gating of MCF7 cells. Singlets were gated where G_1 peak was approximately 300 PI area. Cells that were asynchronous or treated with 500 nM palbociclib for 4 hours or 48 hours were analyzed. Histograms for the different drug treatment show a G1 arrest following 48 hours. (**B**) Same but with MD-MBA-231 cells. (**C**) NIH 3T3 cells that were asynchronous or serum starved (-FBS).

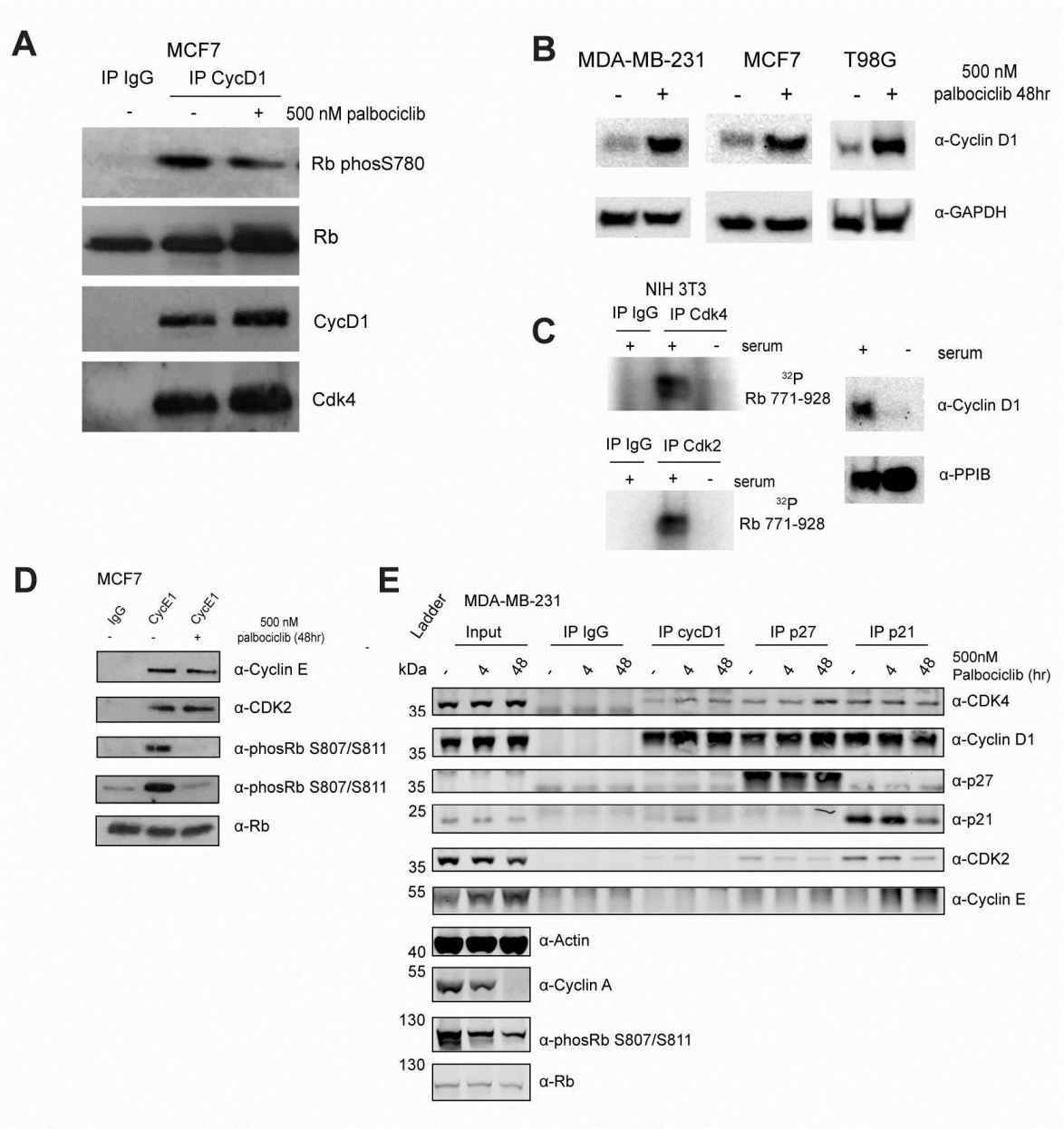

Fig. S12. Data supporting observation of uninhibited CDK4 activity and inhibited CDK2 activity upon palbociclib treatment. (A) Endogenous CycD1 complexes retain kinase activity following treatment of cells with palbociclib. MCF7 cells were treated with 500 nM palbociclib as indicated for 48 hr and lysates were immunoprecipitated with an anti-CycD1 antibody. The immunoprecipitates were used in a kinase assay as in **Fig. 8B** except the phosphorylation of the Rb C-terminus was detected using an S780-phosphospecific Rb antibody. Western blots of total Rb (recombinant C-terminus), CycD1, and CDK4 in the kinase reactions with immunoprecipitated complex are also shown. (**B**) Loading controls for lysates and CycD1 levels in the immunoprecipitates used for **Fig. 8B**. **(C)** Immunoprecipitated CDK4 and CDK2 complexes from serum-starved NIH 3T3 cells lack kinase activity toward exogenous Rb 771-928 substrate. The western blot at the right shows levels of CycD1 and a control protein. (**D**) Kinase activity of CycE1 complexes is diminished upon treatment of cells with palbociclib, despite levels of CDK2 and CycE remaining constant. Extracts were

precipitated with an anti-CycE antibody and phosphorylated Rb was detected with an S807/S811 phospho-specific Rb antibody. We note that similar IP experiments with CycA are not conclusive because CycA levels are depleted in these cells upon palbociclib treatment (**Fig. 8C**) (*53*). (**E**) Changes in CDK complexes that occur upon palbociclib in MDA-MB-231 cells. Same experiments as in MCF cells shown in **Fig. 8C.**

7

Table S1 X-ray crystallography data collection and refinement statistics. Values in parentheses are for highest resolution shell.

	p27-CDK4-CycD1	p21-CDK4-CycD1	phosp27-CDK4-CycD1	p27(3E)-CDK4-CycD1
Data collection				
Space group	$P2_12_12_1$	$P2_122_1$	$P2_12_12_1$	$P2_12_12_1$
Cell dimensions				
a, *b*, *c* (Å)	62.40, 67.48, 187.2	62.6, 67.9, 185.4	62.85, 66.63, 184.24	62.58, 66.73, 184.85
α, β, γ (°)	90, 90, 90	90, 90, 90	90, 90, 90	90, 90, 90
Resolution (Å)	93.64-2.30 (2.42-2.30)	92.68-3.19 (3.41-3.19)	46.06-2.89 (3.07-2.89)	92.42-2.80 (2.95-2.80)
R_{merge}	13.0 (108.2)	16.7 (83.7)	18.8 (99.9)	19.4 (82.6)
R_{pim}	4.8 (40.8)	8.1 (40.6)	5.6 (29.6)	7.7 (31.8)
$I / \sigma I$	9.9 (2.2)	9.2 (2.1)	14.3 (2.9)	8.3 (2.4)
CC 1/2	0.99 (0.68)	0.99 (0.75)	0.99 (0.81)	0.98 (0.78)
Total reflections	274807 (34774)	81814 (14232)	232992 (36095)	139972 (21264)
Unique Reflections	35354 (4854)	13821 (2439)	18044 (2830)	19805 (2851)
Completeness (%)	98.2 (94.5)	99.9 (99.8)	99.8(99.0)	99.8 (99.9)
Redundancy	7.8 (7.2)	5.9 (5.8)	12.9 (12.8)	7.1 (7.5)
Wilson B-factor	35	52	36	38
Refinement				
Resolution (Å)	93.64-2.30	44.70-3.19	45.72-2.89	62.77-2.80
No. reflections	35354 (4854)	13821 (2439)	18044 (2830)	19805 (2851)
R_{work} / R_{free}	17.4/22.1	20.6/25.8	18.9/24.2	22.1/27.5
No. atoms	4709	4388	4498	4408
Protein	4513	4388	4498	4408
Water	194	-	-	-
Refined B-factors (Å^2)				
Overall	57	84	60	55
CDK4	60	89	67	61
CycD1	42	66	41	38
p27	78	119	78	80
water	53	-	-	-
R.m.s. deviations				
Bond lengths (Å)	0.008	0.002	0.005	0.004
Bond angles (°)	1.18	0.50	1.00	0.94
Ramachandran analysis				
Favored (%)	100	98.9	99.64	99.82
Disallowed (%)	0	1.1	0.36	0.18

Table S2. Amino acids built into the final refined structural models. Residues listed in parentheses are included in the protein construct used in the crystal.

Chain	p27-CDK4-CycD1	p21-CDK4-CycD1	phosp27-CDK4-CycD1	p27(3E)-CDK4-CycD1
CDK4	19-79; 84-159; 175-297 (1-303)	18-78; 82-160; 175-297 (1-303)	18-78; 83-159; 176-295 (1-303)	18-78; 82-158; 173-296 (1-303)
CycD1	19-265 (16-267)	19-262 (16-267)	21-264 (16-267)	20-262 (16-267)
p27/p21	25-80 (25-93)	14-67 (14-81)	25-79 (25-106)	25-79 (25-93)